

# Redox-influenced seismic properties of upper-mantle olivine

C. J. Cline<sup>1†</sup>, U. H. Faul<sup>2</sup>, E. C. David<sup>1‡</sup>, A. J. Berry<sup>1</sup> & I. Jackson<sup>1</sup>

**Lateral variations of seismic wave speeds and attenuation (dissipation of strain energy) in the Earth's upper mantle have the potential to map key characteristics such as temperature, major-element composition, melt fraction and water content<sup>1–3</sup>. The inversion of these data into meaningful representations of physical properties requires a robust understanding of the micromechanical processes that affect the propagation of seismic waves<sup>2,3</sup>. Structurally bound water (hydroxyl) is believed to affect seismic properties<sup>2,3</sup> but this has yet to be experimentally quantified. Here we present a comprehensive low-frequency forced-oscillation assessment of the seismic properties of olivine as a function of water content within the under-saturated regime that is relevant to the Earth's interior. Our results demonstrate that wave speeds and attenuation are in fact strikingly insensitive to water content. Rather, the redox conditions imposed by the choice of metal sleeving, and the associated defect chemistry, appear to have a substantial influence on the seismic properties. These findings suggest that elevated water contents are not responsible for low-velocity or high-attenuation structures in the upper mantle. Instead, the high attenuation observed in hydrous and oxidized regions of the upper mantle (such as above subduction zones) may reflect the prevailing oxygen fugacity. In addition, these data provide no support for the hypothesis whereby a sharp lithosphere–asthenosphere boundary is explained by enhanced grain boundary sliding in the presence of water.**

Lattice defects and the structure and composition of grain boundaries in olivine strongly influence the stiffness and strength of the mantle from infinitesimal strains (elastic/anelastic)<sup>4–6</sup>, to large-strain viscous rheology<sup>7</sup>. Central to experimental efforts in quantifying these effects is understanding the influence of hydrogen-related defects on both diffusional and dislocation-governed processes<sup>8,9</sup>. It has been suggested, mainly by analogy with observations of water-enhanced viscous deformation of olivine, that the potential seismological importance of water in the mantle might involve either an increase in defect mobility through increased vacancy populations, or water-enhanced diffusivities facilitating grain boundary sliding<sup>2,10,11</sup>. Substantially modified seismic properties in the presence of water have been observed previously at low frequencies, but only in a single exploratory study conducted under water-saturated conditions<sup>12</sup>. Accordingly, hypotheses concerning water-enhanced grain boundary sliding as an explanation for the sharp lithosphere–asthenosphere boundary<sup>10,11</sup>, and the more general seismological mapping of mantle water contents<sup>2</sup>, remain to be experimentally tested.

Water is conventionally introduced into experimental specimens through the use of solid buffers containing hydrated phases<sup>9</sup>, or as excess fluid, ensuring high water fugacity ( $f_{\text{H}_2\text{O}}$ ) and water-saturated conditions during mechanical testing<sup>9,12</sup>. However, free fluid phases are not expected under upper-mantle conditions. Conducting experiments under a more relevant water-undersaturated environment requires conditions sufficiently oxidizing to ensure that  $f_{\text{H}_2\text{O}} > f_{\text{H}_2}$  (see Methods), for the decoration of intrinsic and extrinsic defects with  $\text{H}^+$ .

A recent experimental campaign<sup>13</sup> used the energetically favoured Ti-clinohumite-like defect ( $\text{Ti-OH}^+$ )<sup>14–16</sup> (Ti located on a metal site, charge balanced by a doubly protonated Si vacancy) to assess the sensitivity of large-strain creep in olivine to small (and undersaturated) water concentrations. A conspicuous modification of large-strain rheology was observed in the presence of low concentrations of this defect, with a near-linear enhancement of strain rate in dislocation creep occurring as a function of increasing hydroxyl content, inferred to be due to the increased concentration of associated Si vacancies<sup>13</sup>.

Motivated by the scant experimental data on the influence of water on seismic properties, here we build upon the work of ref. 13 to explore the micro-strain anelastic effects of changes in  $f_{\text{O}_2}$  and  $f_{\text{H}_2\text{O}}$  that are associated with water-undersaturated conditions. We isostatically hot-pressed, and then mechanically tested under a range of  $f_{\text{O}_2}$  conditions, eight polycrystalline olivine specimens containing different types of hydrated defects in various concentrations. We used different metal sleeves surrounding the olivine specimens during testing to vary the imposed redox conditions<sup>13</sup>—a Pt sleeve to create relatively oxidizing conditions, a  $\text{Ni}_{70}/\text{Fe}_{30}$  ('NiFe') sleeve to produce more-reducing conditions, or a Ni sleeve for an intermediate  $f_{\text{O}_2}$ . The sample suite consisted of undoped and Ti-doped solgel olivine of  $\text{Fo}_{90}$  composition (containing 90% forsterite)<sup>13</sup>, Ti-doped forsterite and a reconstituted San Carlos olivine (see Extended Data Table 1 for sample compositions). Each specimen was mechanically tested in torsional forced oscillation at periods representative of the seismic band (1–1,000 s), using a confining pressure of 200 MPa and temperatures up to 1,200 °C (see Methods for details).

Fourier-transform infrared (FTIR) spectroscopy was used to identify the hydrous defect and quantify the water content of each specimen after mechanical testing. The FTIR spectra (Fig. 1a) of Ti-bearing specimens are dominated by absorption bands at  $3,572\text{ cm}^{-1}$  and  $3,525\text{ cm}^{-1}$ , attributed to the Ti-OH defect<sup>14,15</sup>, for which a site-specific calibration factor<sup>16</sup> was used to infer the concentration of chemically bound hydroxyl. The residual broadband absorbance is attributed to the presence of molecular water, and higher concentrations of molecular water are prominent in Ti-free specimens. Additional hydrated defects associated with Si vacancies (at  $3,612\text{ cm}^{-1}$ ) and trivalent ions (at  $3,350\text{ cm}^{-1}$ ) can also be observed in some specimens. The specimen tested within a NiFe-sleeve shows no absorbance within the range  $4,000\text{--}3,000\text{ cm}^{-1}$ , indicating the absence of both chemically bound hydroxyl and molecular water.

Mechanical data from all specimens exhibit anelastic relaxation typical of the 'absorption band': a monotonic increase of dissipation  $Q^{-1}$  and decrease of shear modulus  $G$  with increasing oscillation period (Fig. 1b, c) and with increasing temperature. Further, the ( $G$ ,  $Q^{-1}$ ) data for each specimen can be adequately described by a Burgers-type creep function<sup>17</sup>. Previous forced oscillation results for a Pt-encapsulated and water-saturated dunite<sup>12</sup> show a broad similarity in shear modulus and dissipation to the similarly sleeved, but water-undersaturated, specimens of this study. Additionally, the global Burgers model<sup>17</sup> for a suite

<sup>1</sup>Research School of Earth Sciences, Australian National University, Canberra, Australian Capital Territory, Australia. <sup>2</sup>Earth Atmospheric and Planetary Sciences, Massachusetts Institute of Technology, Cambridge, Massachusetts, USA. <sup>†</sup>Present address: Department of Earth Sciences, University College London, London, UK.

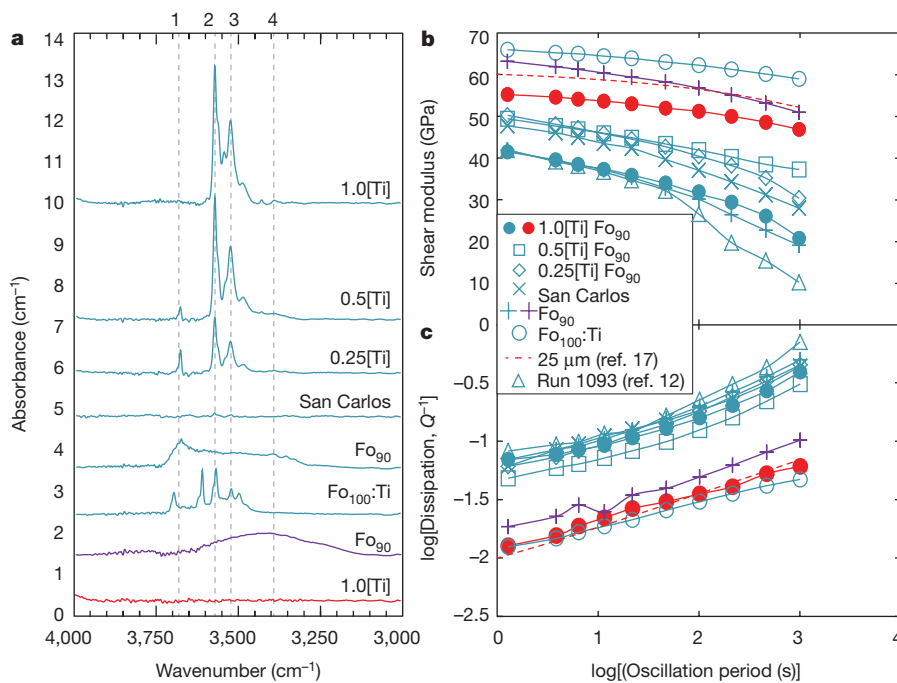


**Figure 1 | Seismic properties of all specimens.** FTIR spectra for all specimens are shown in **a**, with the corresponding shear modulus in **b** and dissipation data in **c** for a representative temperature of 1,100 °C. Pt-sleeved specimens are represented in blue, Ni-sleeved in purple and NiFe-sleeved in red. In **a**, peak (1) represents a secondary hydrous phase at 3,690  $\text{cm}^{-1}$ , peaks (2) and (3) show Ti-OH<sup>14–16</sup> and peak (4) shows OH associated with trivalent ions<sup>14,16</sup>. In **b** and **c**, the Burgers model for dry olivine<sup>17</sup> was evaluated for a grain size of 25  $\mu\text{m}$ , and is shown by

of dry and melt-free  $\text{Fo}_{90}$  polycrystals, updated to fit additional more recent data, closely matches those for the Ti-doped NiFe-sleeved sample tested here, indicating that the presence of the Ti-dopant alone does not affect the observed anelastic relaxation (Fig. 1b).

The dissipation and the associated frequency dependence (dispersion) of the shear modulus are much greater for the Fe-bearing olivine specimens tested within Pt sleeves than for the specimen tested within NiFe (Fig. 1b, c). However, within the suite of Pt-sleeved Fe-bearing polycrystals, the mechanical behaviour is strikingly consistent for specimens ranging widely in concentrations of both bound hydroxyl associated with Ti and molecular water (Fig. 2a). We therefore conclude that the anelastic behaviour of olivine does not vary systematically with either [H/Si], or with Si vacancies associated with the Ti-OH defect, in contrast to the findings of ref. 13 regarding water-enhanced large-strain dislocation creep. In addition, the presence of varying quantities of molecular water (Fig. 2b) and other hydrated defect species also appears to have no effect on the measured seismic properties. Finally, despite the presence of structural water associated with Ti/Mg substitution and Si vacancies, the mechanical properties of the Ti-doped forsterite sample are indistinguishable from those of dry, NiFe-sleeved  $\text{Fo}_{90}$  olivine (Figs 1 and 2)—suggesting that in the absence of Fe, higher  $f_{\text{O}_2}$  and  $f_{\text{H}_2\text{O}}$  conditions are ineffective in enhancing anelastic relaxation.

The magnitude of anelastic relaxation of Fe-bearing olivine presented in Fig. 1b and c instead correlates well with the prevailing  $f_{\text{O}_2}$ , influenced by the respective metal sleeving materials. The  $f_{\text{O}_2}$  conditions were inferred from separate hot-pressing experiments, involving the measurement of Fe partitioning between olivine and widely dispersed fine-grained Pt blebs, and vary between Pt- and NiFe-sleeved solgel olivine specimens by 1.7 logarithmic units. The calculated values of  $f_{\text{O}_2}$  within our large specimens differ from those of the respective metal-oxide buffers, but the expected relative ordering is maintained for the different sleeving materials: for example, Pt > Ni > NiFe (see Methods). Additionally, the  $f_{\text{O}_2}$  of Pt-sleeved San Carlos olivine is 0.9 logarithmic

units higher than pure solgel olivine sleeved within Pt owing to the presence of impurities, such as Ni and Cr<sup>18</sup>. Using the commonly invoked defect charge balance between the concentrations of ferric iron,  $[\text{Fe}_M^*]$ , and metal-site vacancies,  $[\text{V}_M'']$ <sup>19,20</sup>, we find that Pt-sleeved specimens contain concentrations of such defects roughly twice as high as in NiFe-sleeved specimens. The dissipation measured for the Fe-bearing olivine specimens across the entire range of temperatures and oscillation periods is consistent with the relation  $Q^{-1} \approx (f_{\text{O}_2})^{1/3}$  (Fig. 3). Our data clearly demonstrate a previously unrecognized link between  $Q^{-1}$  and redox conditions. The strength of the inferred

the red dashed curves. Data from a water-saturated Anita Bay dunite (experimental run number 1093 in ref. 12) are shown with blue triangles. Ti-doped samples are denoted by the nomenclature  $x[\text{Ti}]$  where  $x$  is the approximate amount of Ti normalized to the sample with the highest Ti-dopant concentration, that is, 800 atom parts per million Ti/Si (Extended Data Table 1). All experimental data are normalized to a common grain size<sup>17</sup> of 25  $\mu\text{m}$ .

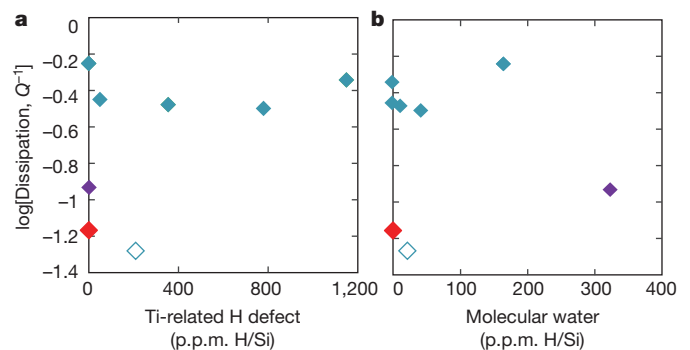


**Figure 2 | Dissipation  $Q^{-1}$  measured at representative conditions of 1,100 °C and 1,000 s oscillation period.** **a**,  $Q^{-1}$  versus the corresponding concentration in atom parts per million (p.p.m.) of Ti-related H/Si. **b**,  $Q^{-1}$  versus the corresponding concentration of molecular water. Colours are as in Fig. 1, with Fe-bearing olivine represented by solid diamonds, and the Ti-doped forsterite specimen represented by the hollow diamond. Dissipation data are normalized to a common grain size of 25  $\mu\text{m}$ . Errors on measurements of dissipation, given by  $\sigma[\log(Q^{-1})] = 0.05$  and water content (standard deviation) are smaller than the symbols used for plotting.

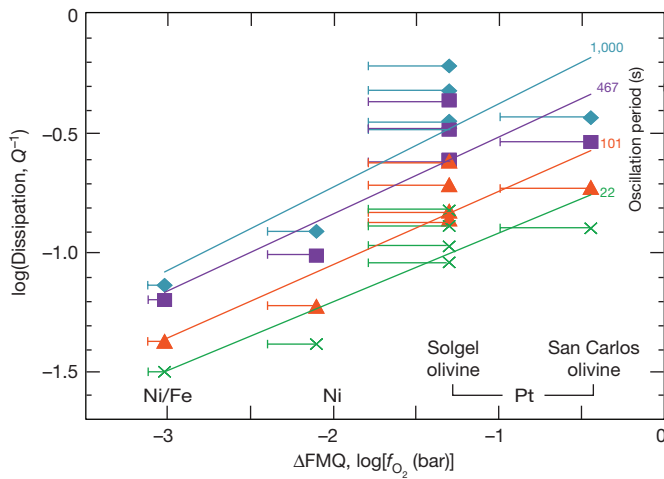


**Figure 3 | Dissipation data at 1,100 °C plotted as a function of  $f_{O_2}$  for different capsule materials and several representative oscillation periods.** Linear fits of the data at the various oscillation periods (coloured numbers) have an average slope of 0.31. Dissipation data are normalized to a common grain size of 25  $\mu\text{m}$ . The lines attached to plotting symbols provide an indication of the combined uncertainty<sup>30</sup> arising from analytical errors and the use of alternative thermodynamic data (see Methods).  $f_{O_2}$  is given as the deviation from that of the fayalite–magnetite–quartz (FMQ) equilibrium. Distinct  $f_{O_2}$  values for Pt-sleeved solgel-derived and San-Carlos-derived olivine specimens are shown.

sensitivity to the variation of  $f_{O_2}$  results from large changes in  $Q^{-1}$  for the relatively small range of  $f_{O_2}$ .

Increased concentrations and mobilities of lattice defects resulting from more oxidizing conditions (specifically  $\text{Fe}^{3+}$  and vacancies on metal sites) and associated increases in lattice and grain-boundary diffusivities are probably the cause of the observed enhancement in anelastic relaxation. Accordingly, under these more oxidizing conditions, the effective grain-boundary viscosity will be reduced, and hence so will the characteristic timescales  $\tau_e$  and  $\tau_M$  (the Maxwell time), which are associated with elastically and diffusively assisted/accommodated grain-boundary sliding, respectively<sup>5</sup>. Indeed, values of  $\tau_M$  determined from the Burgers model fitting<sup>17</sup> of  $(G, Q^{-1})$  data for each specimen vary systematically with  $f_{O_2}$  (Fig. 4). It has been suggested that water contents of 0.1 wt% may decrease  $\tau_e$  by two to four orders of magnitude and thus enhance dissipation for elastically accommodated grain-boundary sliding, potentially explaining the sharp lithosphere–asthenosphere boundary<sup>10,11</sup>. Here we have demonstrated that there exists no such sensitivity of seismic properties to the presence of water under our

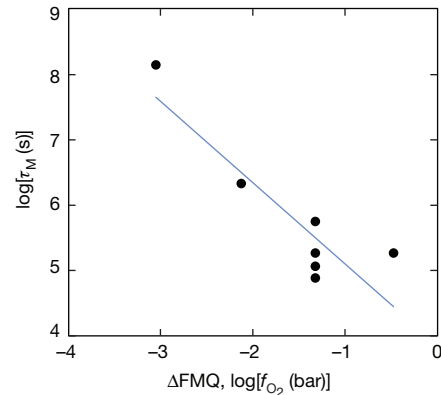


**Figure 4 | Values of  $\log(\tau_M)$  from the refined Burgers model of each  $\text{Fo}_{90}$  olivine specimen plotted as a function of  $f_{O_2}$ .** The data are best-fitted with a line of slope  $-1.2$ .

experimental conditions, but we do observe a comparable enhancement of anelastic relaxation attributable to an increase of  $f_{O_2}$  by 1.7 logarithmic units and the concomitant defects.

Results from the recent NoMelt seismic experiment, which was conducted in 60–80-million-year-old lithosphere in the central Pacific, away from ridges and hotspots<sup>21</sup>, are consistent with our findings of a negligible influence of water on seismic properties. Analyses of basalts from the East Pacific Rise and Macquarie Island indicate that water contents for the Pacific upper mantle approach 200 parts per million by weight  $\text{H}_2\text{O}$  (ref. 22, and references therein). Taking partitioning of the bulk water content between olivine and pyroxenes into account, olivine in the upper mantle may thus contain approximately 400–1,000 atom parts per million  $\text{H}/\text{Si}$ <sup>23,24</sup> (that is, within the range experimentally investigated here). In addition, electrical conductivity measurements collected as part of the NoMelt experiment indicate increased conductivity in the asthenosphere, consistent with water contents of 25–400 parts per million by weight<sup>25</sup>. The presence of this amount of water was previously expected to reduce seismic velocities substantially<sup>2,10</sup>. However, the results of the NoMelt survey<sup>21</sup> indicate that the observed velocity structure, including the velocity minimum, can be explained with a relatively minor additional enhancement of the anelastic relaxation characteristics of dry and relatively reduced olivine<sup>17</sup>, down to a depth of 300 km, that is, well below the melt (and volatile) extraction horizon (Fig. 5).

In contrast, the low velocity and high attenuation observed above subducting slabs are typically attributed to volatile release (and therefore higher water contents<sup>26</sup>) and to the presence of melt<sup>3</sup>. However,

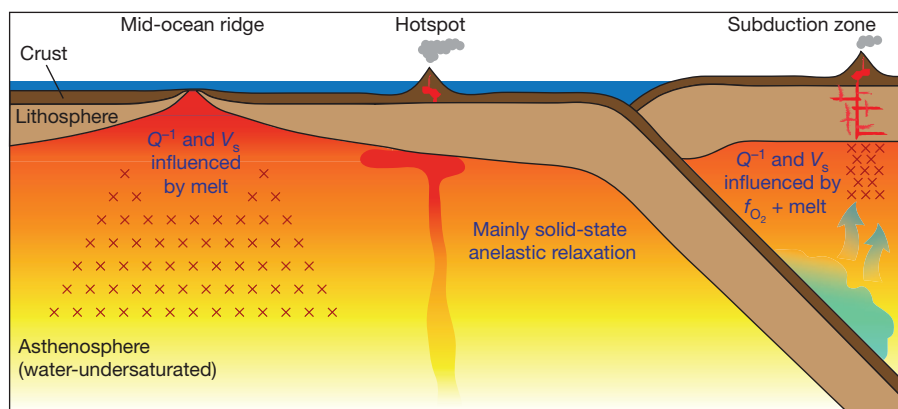


**Figure 5 | Dominant influences on anelastic relaxation responsible for the reduced seismic shear-wave velocities and attenuation of seismic waves.** ‘Normal’ asthenosphere beneath old oceanic lithosphere, which is water-undersaturated and contains only a very minor melt fraction, is subject mainly to solid-state anelastic relaxation. Higher melt fractions in

mid-ocean ridge environments result in enhanced relaxation through the partial wetting of grain boundaries (red crosses indicate the presence of appreciable melt), whereas mantle-wedge environments are influenced by both the presence of melt and increased oxygen fugacity,  $f_{O_2}$ . Blue text lists the influences on seismic shear-wave velocities  $V_s$  and attenuation.

measurements of the ratio between ferric iron and total iron ( $\text{Fe}^{3+}/\Sigma\text{Fe}$ ) in arc lavas indicate that  $f_{\text{O}_2}$  is also higher by 1–1.5 logarithmic units in the mantle wedge in comparison to adjacent oceanic lithosphere<sup>27–29</sup>. With the  $Q^{-1} \approx (f_{\text{O}_2})^{1/3}$  result of this study, such variations of  $f_{\text{O}_2}$  are predicted to enhance dissipation 2–3-fold, with the associated dispersion reflected in reduced wave speeds. Therefore, although water content generally correlates with magmatic ratios<sup>27</sup> of  $\text{Fe}^{3+}/\Sigma\text{Fe}$ , and may also increase grain size<sup>3</sup>, the reduced velocities and increased attenuation above subducting slabs may be attributable not to the presence of fluids or hydrated defects, but rather to the prevailing redox conditions and the presence of melt (Fig. 5).

**Online Content** Methods, along with any additional Extended Data display items and Source Data, are available in the online version of the paper; references unique to these sections appear only in the online paper.

**Received 4 August 2017; accepted 4 January 2018.**

- Romanowicz, B. A. & Mitchell, B. J. in *Treatise on Geophysics* 2nd edn, 789–827 (Elsevier, 2015).
- Karato, S. Mapping water content in upper mantle. In *Inside the Subduction Factory* Vol. 138, 135–152 (Geophysical Monograph Series, AGU, 2003).
- Abers, G. et al. Reconciling mantle attenuation-temperature relationships from seismology, petrology, and laboratory measurements. *Geochem. Geophys.* **15**, 3521–3542 (2014).
- Jacobsen, S. D. et al. Effects of hydration on the elastic properties of olivine. *Geophys. Res. Lett.* **35**, L14303 (2008).
- Jackson, I. in *Treatise on Geophysics* 2nd edn, 539–571 (Elsevier, 2015).
- Farla, R. J., Jackson, I., Fitz Gerald, J. D., Faul, U. H. & Zimmerman, M. E. Dislocation damping and anisotropic seismic wave attenuation in Earth's upper mantle. *Science* **336**, 332–335 (2012).
- Bai, Q., Mackwell, S. J. & Kohlstedt, D. L. High-temperature creep of olivine single crystals 1. Mechanical results for buffered samples. *J. Geophys. Res.* **96**, 2441 (1991).
- Karato, S.-I. & Jung, H. Effects of pressure on high-temperature dislocation creep in olivine. *Phil. Mag.* **83**, 401–414 (2003).
- Mei, S. & Kohlstedt, D. Influence of water on plastic deformation of olivine aggregates. 2. Diffusion creep regime. *J. Geophys. Res.* **105**, 21457–21469 (2000).
- Karato, S.-I. On the origin of the asthenosphere. *Earth Planet. Sci. Lett.* **321/322**, 95–103 (2012).
- Olugboji, T. M., Karato, S.-I. & Park, J. Structures of the oceanic lithosphere-asthenosphere boundary: mineral-physics modeling and seismological signatures. *Geochem. Geophys.* **14**, 880–901 (2012).
- Aizawa, Y. et al. Seismic properties of Anita Bay dunite: an exploratory study of the influence of water. *J. Petrol.* **49**, 841–855 (2008).
- Faul, U. H., Cline, C. J. II, David, E. C., Berry, A. J. & Jackson, I. Titanium-hydroxyl defect-controlled rheology of the Earth's upper mantle. *Earth Planet. Sci. Lett.* **452**, 227–237 (2016).
- Berry, A. J., Hermann, J., O'Neill, H. S. C. & Foran, G. J. Fingerprinting the water site in mantle olivine. *Geology* **33**, 869 (2005).
- Walker, A. M., Hermann, J., Berry, A. J. & O'Neill, H. S. C. Three water sites in upper mantle olivine and the role of titanium in the water weakening mechanism. *J. Geophys. Res.* **112**, B05211 (2007).
- Kovács, I., O'Neill, H. S. C., Hermann, J. & Hauri, H. Site-specific infrared OH absorption coefficients for water substitution into olivine. *Am. Mineral.* **95**, 292–299 (2010).
- Jackson, I. & Faul, U. H. Grain-size sensitive viscoelastic relaxation in olivine: Towards a robust laboratory-based model for seismological application. *Phys. Earth Planet. Inter.* **183**, 151–163 (2010).
- De Hoog, J., Gail, L. & Cornell, D. Trace-element geochemistry of mantle olivine and application to mantle petrogenesis and geothermobarometry. *Chem. Geol.* **270**, 196–215 (2010).
- Nakamura, A. & Schmalzried, H. On the nonstoichiometry and point defects of olivine. *Phys. Chem. Mineral.* **10**, 27–37 (1983).
- Dohmen, R. & Chakraborty, S. Fe–Mg diffusion in olivine II: point defect chemistry, change of diffusion mechanisms and a model for calculation of diffusion coefficients in natural olivine. *Phys. Chem. Mineral.* **34**, 409–430 (2007).
- Lin, P.-Y. P. et al. High-resolution seismic constraints on flow dynamics in the oceanic asthenosphere. *Nature* **535**, 538–541 (2016).
- Shimizu, K. et al. Two-component mantle melting-mixing model for the generation of mid-ocean ridge basalts: implications for the volatile content of the Pacific upper mantle. *Geochim. Cosmochim. Acta* **176**, 44–80 (2016).
- Hirth, G. & Kohlstedt, D. L. Water in the oceanic upper mantle: implications for rheology, melt extraction and the evolution of the lithosphere. *Earth Planet. Sci. Lett.* **144**, 93–108 (1996).
- Tenner, T. J., Hirschmann, M. M., Withers, A. C. & Ardia, P. H<sub>2</sub>O storage capacity of olivine and low-Ca pyroxene from 10 to 13 GPa: consequences for dehydration melting above the transition zone. *Contrib. Mineral. Petrol.* **163**, 297–316 (2012).
- Sarafian, E. et al. The electrical structure of the central Pacific upper mantle constrained by the NoMelt experiment. *Geochem. Geophys.* **16**, 1115–1132 (2015).
- Stachnik, J. C., Abers, G. A. & Christensen, D. H. Seismic attenuation and mantle wedge temperatures in the Alaska subduction zone. *J. Geophys. Res.* **109**, B10304 (2004).
- Kelley, K. A. & Cottrell, E. Water and the oxidation state of subduction zone magmas. *Science* **325**, 605–607 (2009).
- Brounce, M. N., Kelley, K. A. & Cottrell, E. Variations in  $\text{Fe}^{3+}/\Sigma\text{Fe}$  of Mariana arc basalts and mantle wedge  $f_{\text{O}_2}$ . *J. Petrol.* **55**, 2513–2536 (2014).
- McCammon, C. A. et al. Oxidation state of iron in hydrous mantle phases: implications for subduction and mantle oxygen fugacity. *Phys. Earth Planet. Inter.* **143–144**, 157–169 (2004).
- Faul, U. H., Cline, C. J. II, Berry, A., Jackson, I. & Garapic, G. Constraints on oxygen fugacity within metal capsules. *Phys. Chem. Mineral.* <https://doi.org/10.1007/s00269-017-0937-7> (2017).

**Acknowledgements** We thank H. Kokkonen and H. Miller for technical support with sample preparation and operation of the Australian National University rock physics laboratory, H. Chen for assistance with electron backscatter diffraction, and S. Karato of Yale University for suggestions that improved the manuscript. This work was supported by grant DP130103848 from the Australian Research Council to I.J., A.J.B., U.H.F. and S. Karato. U.H.F. acknowledges support from NSF grant EAR 1321889. C.J.C. gratefully acknowledges funding by an Australian National University International PhD Research Scholarship.

**Author Contributions** C.J.C. conducted the forced-oscillation measurements (with contributions from E.C.D.). C.J.C. obtained the microstructural and spectroscopic data, subsequently interpreted by U.H.F., E.C.D., I.J., A.J.B. and C.J.C.  $f_{\text{O}_2}$  and  $\text{Fe}^{3+}$  calculations were performed by U.H.F. The manuscript was written by C.J.C. with contributing revisions and discussion from all authors.

**Author Information** Reprints and permissions information is available at [www.nature.com/reprints](http://www.nature.com/reprints). The authors declare no competing financial interests. Readers are welcome to comment on the online version of the paper. Publisher's note: Springer Nature remains neutral with regard to jurisdictional claims in published maps and institutional affiliations. Correspondence and requests for materials should be addressed to C.J.C. ([christopher.cline@anu.edu.au](mailto:christopher.cline@anu.edu.au)).

**Reviewer Information** *Nature* thanks G. Abers and T. Irifune for their contribution to the peer review of this work.

## METHODS

**Specimen fabrication.** Three types of starting materials were used to produce the eight olivine specimens tested in this study. Seven specimens were fabricated from precursor powder prepared by a solution-gelation process (two undoped  $\text{Fo}_{90}$ , four Ti-doped  $\text{Fo}_{90}$  and one Ti-doped  $\text{Fo}_{100}$ ), and the other from powder produced by crushing hand-picked San Carlos olivine phenocrysts. The fabrication procedure for the different solgel-derived olivine powders follows the methodology of ref. 31 for  $\text{Fo}_{90}$  and of ref. 13 for the Ti-doped forsterite material. Nitrates of Fe and Mg (and tetra-ethoxy orthotitanate for the Ti-bearing material) were mixed with a nonstoichiometric amount of tetraethyl orthosilicate to ensure that the final olivine was orthopyroxene-saturated. Gelation of this mix was initiated with a small amount of  $\text{HNO}_3$ , followed by dehydration, and firing in air within a Pt crucible to remove all nitrate. The resulting powders were subjected to multiple firings in a 1-atm furnace in a 50:50  $\text{CO}-\text{CO}_2$  gas mix at 1,400 °C for 16 h, with intervening grindings to produce a pure and homogeneous starting material with an average grain diameter of about 1  $\mu\text{m}$ . The San Carlos precursor material is identical to that fabricated and used by ref. 32.

The precursor powder was then cold-pressed at about 10 MPa into a set of five 3-g pellets that were fired in an atmosphere of 50:50  $\text{CO}-\text{CO}_2$  gas for 16 h at either 1,400 °C for the solgel-derived or 1,300 °C for the San-Carlos-derived material. The stack of five pellets was accommodated within a laser-welded Pt capsule, sandwiched between alumina pistons within a thin-walled mild steel jacket and hot-pressed at 1,200 °C and 300 MPa for 24 h in a Paterson internally heated gas-medium pressure vessel. Specimens were recovered by dissolving the steel jacket in  $\text{HNO}_3$  and subsequently peeling off the remaining Pt capsule. Transverse sections were cut about 1.5 mm from the end of each sample for microstructural analysis, with the bulk of the specimens then being precision ground to a right cylindrical shape with a diameter of 11.5 mm and lengths ranging between 31 mm and 33 mm. Each such specimen was then fired at 600 °C in Ar to remove all traces of organic lubrication used in the grinding, and held in a drying oven at 110 °C until mechanical testing.

**Mechanical testing.** Mechanical testing of each specimen, via forced torsional oscillation, was conducted using the modified Paterson gas-medium apparatus originally described by ref. 33, and later with updated procedures reported by ref. 34. Specimens were sleeved in either Pt,  $\text{Ni}_{70}\text{Fe}_{30}$  or Ni foil and placed inside a mild-steel jacket along with Lucalox alumina torsion rods. Pressure was applied via Ar, and maintained at 200 MPa for the duration of the experiment to load all interfaces (such as those between the sample and the aluminium oxide torsion rods) within the experimental assembly, and thereby to ensure appropriate frictional coupling. The temperature was increased to 1,200 °C, and maintained for a time interval ranging between 23 h and 45 h, during which the mechanical response was monitored until steady and repeatable values of normalized compliance and phase lag were observed, indicating that the evolution of the microstructure and chemical environment is complete. Since this evolution is thermally activated, once steady-state mechanical response is achieved at the highest temperature, continued mechanical testing during the slow staged cooling (over approximately 1 week) is thought to be representative of a single chemical environment and microstructure.

Torsional testing involves the application of a sinusoidal stress at each of ten oscillation periods, logarithmically equi-spaced between 1 s and 1,000 s. Maximum strains at the highest temperature and longest oscillation period were kept to  $<10^{-5}$  to ensure linear behaviour, which was confirmed before beginning the formal test at the highest temperature by halving the strain amplitude and monitoring values of  $Q^{-1}$ . A complete experiment encompasses testing at oscillation periods of 1–1,000 s followed by a complementary torsional microcreep test, which is intended to assess the recoverability of the viscoelastic strain<sup>33</sup>. After both types of torsional tests were complete, the temperature was reduced by 50 °C, and the procedure was repeated until nearly elastic behaviour was observed, upon which the temperature interval was increased to 100 °C, until room temperature was reached.

**Water content and grain-size analysis.** Water content was determined using FTIR, for both the hot-pressed precursor and for specimens recovered after mechanical testing. Spectra were recorded using unpolarized light from 400- $\mu\text{m}$ -thick traverse sections with an apertured spatial resolution of 200  $\mu\text{m} \times 200 \mu\text{m}$  using a Bruker Hyperion 2000 microscope and a Tensor 27 spectrometer with a MCT-A detector. Samples were placed in a Plexiglas box and purged with dry air for 45 min before, and continually during, spectral acquisition. Each spectrum is the average of 64 scans, recorded between 600  $\text{cm}^{-1}$  and 5,000  $\text{cm}^{-1}$  with a resolution of 4  $\text{cm}^{-1}$ .

Determination of water content follows the method of ref. 13, in which a site-specific calibration factor of  $k = 0.18$  is used to convert the integrated area between 3,450  $\text{cm}^{-1}$  and 3,600  $\text{cm}^{-1}$  into the concentration of crystallographically bound hydroxyl. The residual broadband absorption is attributed to the presence of molecular water<sup>16</sup>, and is quantified separately using the magnitude of absorbance at 3,450  $\text{cm}^{-1}$  and a molar absorption coefficient of 115  $\text{mol}^{-1} \text{cm}^{-1}$ . An unidentified secondary hydrous phase identified in the FTIR spectra of some specimens will not affect the quoted water contents or the measured mechanical properties. Presumably this phase formed during the slow staged cooling, and

because hydrated phases are unstable above 700 °C<sup>35</sup> and anelasticity is not appreciable or measurable below this temperature, this hydrous phase will not affect the mechanical response of the specimens. The presence of such a hydrous phase is suggestive of a hydrous environment during mechanical testing, even in the absence of any other structural H-related defects.

Electron back-scatter diffraction lattice orientation maps were collected to determine the grain size of each specimen after mechanical testing. Sections were successively polished down from 800-grit silicon carbide to a final vibratory polish using 0.05  $\mu\text{m}$  colloidal silica. Orientation maps were collected at the Center for Advanced Microscopy at Australian National University using a Zeiss Ultra Plus field-emission scanning electron microscope fitted with an Oxford Nordlys S electron back-scatter diffraction camera. A representative orientation map is available in Extended Data Fig. 1.

**Determination of  $f_{\text{O}_2}$  and  $\text{Fe}^{3+}$  in olivine.** The oxygen fugacity  $f_{\text{O}_2}$  was determined for the differently sleeved olivine specimens through separate hot-pressing experiments. 1 wt% Pt-black was mixed with either solgel-derived or San-Carlos-derived olivine powder; then the material was encapsulated in either Pt, Ni, NiFe or Fe foil and hot-pressed in a Paterson internally heated gas apparatus at 1,200 °C and 300 MPa for 24 h. The recovered specimens were then analysed using standardized energy-dispersive X-ray spectroscopy and electron microprobe wavelength-dispersive spectroscopy analysis to yield the Fe contents of both the small Pt particles (about 10  $\mu\text{m}$ ) and of the surrounding olivine. Using the metal activities  $\gamma$  in both the olivine and alloyed Pt blebs, this then results in a calculable<sup>36</sup>  $f_{\text{O}_2}$  value, using the relation<sup>37</sup>:

$$\log(f_{\text{O}_2}) = 2\log(\gamma_{\text{Fe}}^{\text{ol}}) - 2\log(\gamma_{\text{Fe}}^{\text{alloy}}) + 2\log(X_{\text{Fe}}^{\text{ol}}/X_{\text{Fe}}^{\text{alloy}}) - \log(a_{\text{SiO}_2}) - \log(K_2)$$

where  $a_{\text{SiO}_2}$  is silica activity,  $X_{\text{Fe}}$  is the mole fraction of Fe either in the olivine or in the Pt blebs and  $K_2$  is the appropriate equilibrium constant. The activity of Fe in olivine is calculated as in ref. 37:

$$\ln(\gamma_{\text{Fe}}^{\text{ol}}) = (1 - X_{\text{Fe}}^{\text{ol}})^2(600 + 0.0013P)/T$$

where  $P$  is pressure and  $T$  is absolute temperature. The activity of Fe in the PtFe metal alloy is calculated from ref. 36:

$$\ln\gamma_{\text{Fe}}^{\text{alloy}} = [W_{\text{G1}} + 2(W_{\text{G2}} - W_{\text{G1}})X_{\text{Fe}}^{\text{alloy}}](X_{\text{Fe}}^{\text{alloy}})^2/RT$$

where  $W_{\text{G1}} = 138 \text{ kJ mol}^{-1}$  and  $W_{\text{G2}} = 90.8 \text{ kJ mol}^{-1}$  are the Margules parameters and  $R$  is the gas constant. An earlier model for the activity of Fe in the alloy<sup>37,38</sup> resulted in lower calculated values of  $f_{\text{O}_2}$ , particularly for oxidizing conditions; these uncertainties are indicated by the lines in Fig. 3. A detailed analysis of these additional hot-pressing experiments designed for the determination of  $f_{\text{O}_2}$  in large solid samples is available in ref. 30.

Using equations (3) to (5) of ref. 20 (see also references therein), in combination with the appropriate  $f_{\text{O}_2}$  as calculated above, we can determine the concentrations of  $\text{Fe}^{3+}$  (that is,  $[\text{Fe}_M^*]$ ) in our Pt- and NiFe-sleeved specimens. Using the charge neutrality conditions of olivine, we can also determine the concentration of the metal-site vacancies  $[\text{V}_M'']$  in our Pt- and NiFe-sleeved specimens. Olivine at Si-saturated conditions (coexisting with pyroxene) possesses a concentration of  $\text{Fe}^{3+}$  defects described by:

$$\log[\text{Fe}_M^*] = \frac{1}{6}(\log K_x + 2\log 2 + 4\log X_{\text{Fa}}^{\text{ol}} + \log f_{\text{O}_2} + \log a_{\text{SiO}_2})$$

where  $\log K_x = -7.32 - (90,000/2.303RT)$  (ref. 19),  $T$  is in kelvin and  $X_{\text{Fa}}$  is fayalite content. From this calculation of  $[\text{Fe}_M^*]$ , the ratio of  $\text{Fe}^{3+}$  to total Fe can be accessed via the relation:

$$\text{Fe}^{3+}/\Sigma\text{Fe} = \frac{[\text{Fe}_M^*]}{2X_{\text{Fa}}^{\text{ol}}}$$

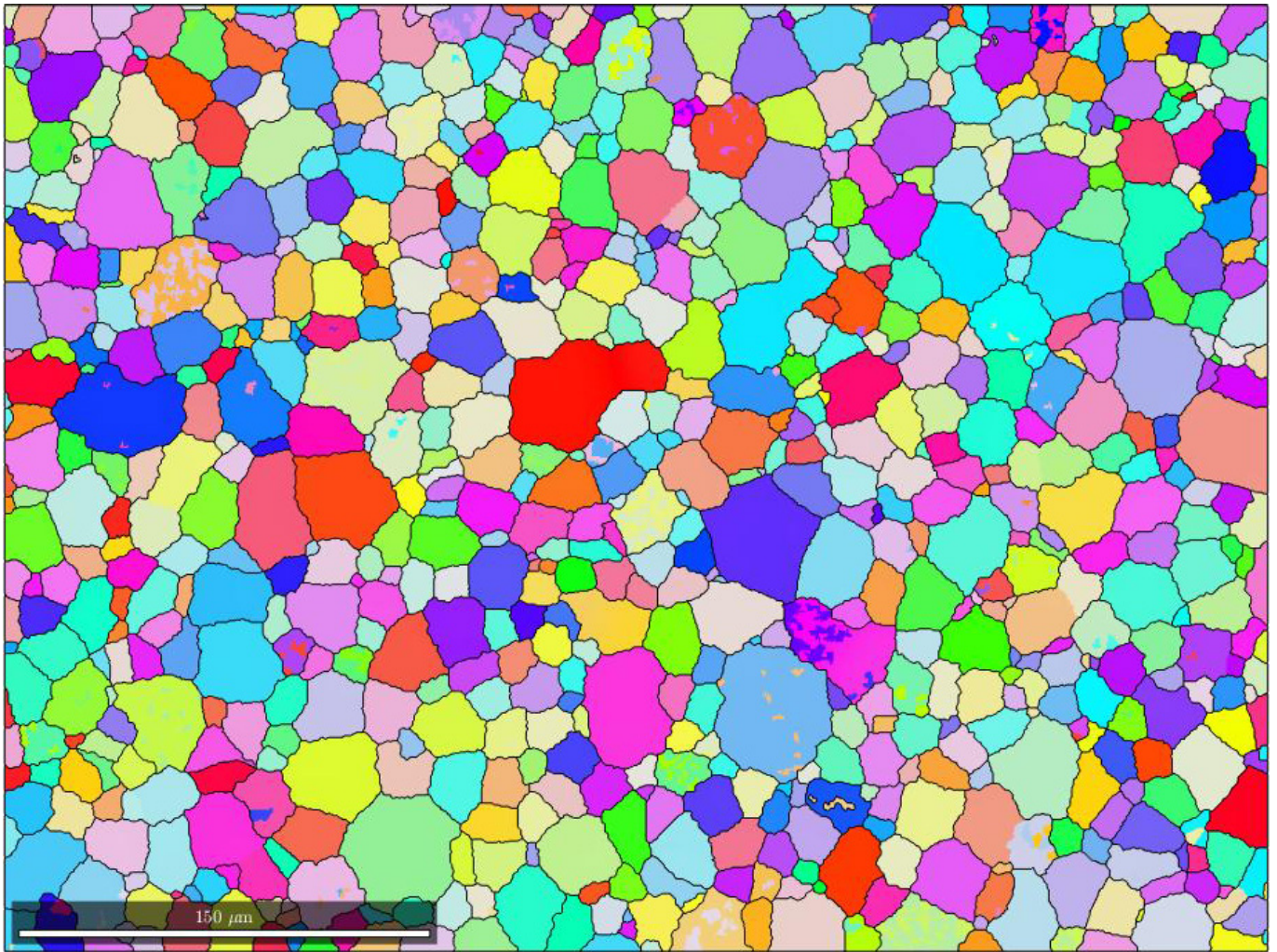
The calculated  $\text{Fe}^{3+}$  percentage of total Fe for Pt-sleeved olivine is 0.17 in the interior. NiFe-sleeved specimens exhibit roughly half of this latter value at  $\text{Fe}^{3+} = 0.09\%$ , and Ni-sleeved olivine is intermediate with 0.13%.

**Hydrogen speciation and water retention as a function of redox conditions.** Water present in our forced-oscillation experiments is not intentionally added. The source of water is presumed to be either via adsorption of moisture within the specimen after removal from the gas mixing furnace and before pressurization or via ingress of H from the relatively reducing furnace environment into the more oxidizing environment within the specimen. Given the evident availability of H in our experiments, the presence of hydrated defects can be controlled through the use of different metal-sleeving materials, imposing either favourable or unfavourable redox conditions for the oxidation of H.

The relative fugacities of  $H_2$  and  $H_2O$  are controlled by the equilibrium  $H_2 + 1/2O_2 = H_2O$  with an equilibrium constant  $K_w$  of 5.9 at 1,200 °C (ref. 39). Using the values of  $f_{O_2}$  determined from the separate hot-pressing experiments detailed above, the difference of +1.7 logarithmic units in  $f_{O_2}$  between NiFe- and Pt-sleeved olivine thus increases the value of  $f_{H_2O}/f_{H_2} = K_w(f_{O_2})^{1/2}$  from only 2.4 to 13.5 (where  $f_{O_2}$  is in units of bar), which is consistent with the inferred dominance of oxidized hydrogen within Pt sleeves, and the loss of water as hydrogen from NiFe-sleeved olivine.

**Data availability.** Source data for Figs 1–4 are provided with the online version of the paper.

31. Jackson, I. *et al.* Grain-size-sensitive seismic wave attenuation in polycrystalline olivine. *J. Geophys. Res.* **107**, 2360 (2002).
32. Tan, B. H., Jackson, I. & Fitz Gerald, J. D. High-temperature viscoelasticity of fine-grained polycrystalline olivine. *Phys. Chem. Miner.* **28**, 641–664 (2001).
33. Jackson, I. & Paterson, M. S. A high pressure, high temperature apparatus for studies of seismic wave dispersion and attenuation. *Pure Appl. Geophys.* **141**, 445–466 (1993).
34. Jackson, I., Barnhoorn, A., Aizawa, Y. & Saint, C. Improved procedures for the laboratory study of high-temperature viscoelastic relaxation. *Phys. Earth Planet. Inter.* **172**, 104–115 (2009).
35. Engi, M. & Lindsley, D. H. Stability of titanian clinohumite: Experiments and thermodynamic analysis. *Contrib. Mineral. Petrol.* **72**, 415–424 (1980).
36. Kessel, R., Beckett, J. R. & Stolper, E. M. Thermodynamic properties of the Pt-Fe system. *Am. Mineral.* **86**, 1003–1014 (2001).
37. Rubie, D. C., Karato, S., Yan, H. & O'Neill, H. S. C. Low differential stress and controlled chemical environment in multianvil high-pressure experiments. *Phys. Chem. Mineral.* **20**, 315–322 (1993).
38. Heald, E. Thermodynamics of iron-platinum alloys. *Trans. Metal. Soc. AIME* **239**, 1337–1340 (1967).
39. Paterson, M. The thermodynamics of water in quartz. *Phys. Chem. Mineral.* **13**, 245–255 (1986).



**Extended Data Figure 1 | Electron back-scatter diffraction map of sample 1623 (0.5[Ti]) after mechanical testing, coloured to indicate different crystallographic orientations. A near-‘foam’ microstructure**

is present, with apparent grain-boundary serrations being an artefact of the post-processing grain boundary reconstruction using MTEX software (<http://mtex-toolbox.github.io/>).

Extended Data Table 1 | Summary of sample characteristics

Sample	Precursor material	Normalized [Ti] <sup>a</sup>	Ti content	Metal sleeve	Bound hydroxyl <sup>c</sup>	Grain size, $\mu\text{m}^{\text{d}}$	$\Delta\text{FMQ}^{\text{e}}$ interior <sup>e</sup>
1515	Fo <sub>90</sub> Solgel	1	802(4) <sup>b</sup>	Pt	1150(190)	25.4(9)	-1.3(5)
1579	Fo <sub>90</sub> Solgel	1	802(4) <sup>b</sup>	Ni <sub>70</sub> Fe <sub>30</sub>	0	25.0(10)	-3.0(1)
1623	Fo <sub>90</sub> Solgel	0.5	396(1) <sup>b</sup>	Pt	780(36)	18.6(6)	-1.3(5)
1637	Fo <sub>90</sub> Solgel	0.25	176(1) <sup>b</sup>	Pt	355(32)	19.9(8)	-1.3(5)
1646	San Carlos	N/A	18-46 <sup>f</sup>	Pt	50(17)	80.9(20)	-0.4(7)
1651	Fo <sub>90</sub> Solgel	0	0	Pt	0	20.6(5)	-1.3(5)
1684	Fo <sub>100</sub> Solgel	1	800(5)	Pt	200(7)	8.2(6)	-0.9
1689	Fo <sub>90</sub> Solgel	0	0	Ni	0	10.7(5)	-2.0(3)

<sup>a</sup>Samples are denoted by the nomenclature x[Ti] where x is the nominal amount of Ti normalized to the sample with the highest Ti-dopant concentration. The values of x are given in this column and correspond to the intended composition.

<sup>b</sup>Atom parts per million Ti/Si determined by LA-ICPMS. Values in parentheses are standard errors of the mean (%).

<sup>c</sup>Atom parts per million H/Si by FTIR in the sample interior, associated with Ti-clinohumite-like defects only. Values in parentheses indicate one standard deviation of data collected on longitudinal maps or radial (linear) transects.

<sup>d</sup>Calculated using electron back-scatter diffraction orientation maps in combination with MTEX processing software. Errors represent the raster step size of the orientation map.

<sup>e</sup>In units of  $\log[f_{\text{O}_2}$  (bar)]. The combined uncertainty is calculated from analytical errors and the use of alternative thermodynamic data for Fe-bearing specimens; see Methods for additional details.

<sup>f</sup>From ref. 18.